



**QUEEN'S  
UNIVERSITY  
BELFAST**

## **A compact single-layer reflective metasurface for high-efficiency polarisation conversion applications in C and X bands**

Raziul Islam, K. M., Rahimian, A., Machado, G. G., Babar Abbasi, M. A., Cheema, A. A., & Meenan, B. J. (2024). A compact single-layer reflective metasurface for high-efficiency polarisation conversion applications in C and X bands. *IET Microwaves, Antennas and Propagation*. Advance online publication. <https://doi.org/10.1049/mia2.12465>

### **Published in:**

IET Microwaves, Antennas and Propagation

### **Document Version:**

Publisher's PDF, also known as Version of record

### **Queen's University Belfast - Research Portal:**

[Link to publication record in Queen's University Belfast Research Portal](#)

### **Publisher rights**

Copyright 2024 the authors.

This is an open access article published under a Creative Commons Attribution License (<https://creativecommons.org/licenses/by/4.0/>), which permits unrestricted use, distribution and reproduction in any medium, provided the author and source are cited.

### **General rights**

Copyright for the publications made accessible via the Queen's University Belfast Research Portal is retained by the author(s) and / or other copyright owners and it is a condition of accessing these publications that users recognise and abide by the legal requirements associated with these rights.

### **Take down policy**





The Research Portal is Queen's institutional repository that provides access to Queen's research output. Every effort has been made to ensure that content in the Research Portal does not infringe any person's rights, or applicable UK laws. If you discover content in the Research Portal that you believe breaches copyright or violates any law, please contact [openaccess@qub.ac.uk](mailto:openaccess@qub.ac.uk).

### **Open Access**

This research has been made openly available by Queen's academics and its Open Research team. We would love to hear how access to this research benefits you. – Share your feedback with us: <http://go.qub.ac.uk/oa-feedback>

## ORIGINAL RESEARCH

# A compact single-layer reflective metasurface for high-efficiency polarisation conversion applications in C and X bands

Kd. M. Raziul Islam<sup>1</sup> | Ardavan Rahimian<sup>1</sup>  | Gabriel G. Machado<sup>1</sup>  |  
Muhammad Ali Babar Abbasi<sup>2</sup>  | Adnan Ahmad Cheema<sup>1</sup>  | Brian J. Meenan<sup>1</sup>

<sup>1</sup>School of Engineering, Ulster University, Belfast, UK

<sup>2</sup>Institute of Electronics, Communications, and Information Technology, Queen's University Belfast, Belfast, UK

**Correspondence**

Ardavan Rahimian.

Email: [a.rahimian@ulster.ac.uk](mailto:a.rahimian@ulster.ac.uk)

**Abstract**

The authors design and experimentally analyse an anisotropic metasurface for the simultaneous conversions of linear cross and circular polarisations in the C and partial X bands. The proposed compact structure utilises a dual-cut square-ring resonator and a square patch on an FR4 substrate above a ground plane. The full-wave simulations exhibit over 92% efficiency in cross-conversion over a fractional bandwidth (BW) of 52.3%. The proposed metasurface efficiently converts linear to circular polarisation in two different bands, achieving left-hand circularly polarised and right-hand circularly polarised efficiencies exceeding 93% and 89%, respectively. The compact unit-cell with dimension  $0.22\lambda \times 0.22\lambda$  attains stable polarisation transformation efficiency rates exceeding 80% up to  $40^\circ$  incident angles. The design is adaptable for efficient wide BW across both lower and higher (millimetre-wave) frequencies through scaling. A prototype of the proposed polarisation converter (PC) was realised and validated effectively in measurements, aligning well with simulations. This PC features a novel and simple structure with multifunctional wideband operation, stable incident angle output, polarisation insensitivity, and scalability, making it an efficient front-end for various radio frequency applications, including polarisation control and polarisation transformers.

**KEYWORDS**

electromagnetic wave polarisation, electromagnetic wave propagation, electromagnetic wave reflection, microwave measurement, microwave metamaterials, planar antennas

## 1 | INTRODUCTION

Polarisation is the oscillation of an electric field in a plane perpendicular to the direction of radio frequency (RF) propagation [1]. Polarisation alignment must be taken into account to regulate or control electromagnetic (EM) waves for a range of practical applications, for example, radars, antennas, and satellite systems [2–4]. Conventional polarisation converters (PCs) are built using Faraday's and birefringence effects [5]. These methods commonly experience large volumes, high losses, and limited bandwidth (BW), undermining their practical applications [6, 7]. To overcome the limitations and drawbacks, metasurface (MS)-based techniques have received considerable attention owing to their ease of realisation and

practicality [8–10]. Some MS-PCs present vast wave manipulation operations by altering material properties and tuning the unit-cell geometry [11, 12]. The unit-cells for polarisation conversion, as the core building blocks, work in transmission [13, 14] or reflection [15, 16] modes, and are of asymmetric types [17–21]. Also, asymmetric or anisotropic cross-polarisation converters (CPCs) in the single or multilayer forms have been reported to operate in both dual and single bands [22–29].

For the linear-to-circular polarisation (LTCP) conversion, various single and multilayer designs have been studied for both reflection [10, 30, 31] and transmission modes [32–34]. However, the PCs reported can effectively perform only one operation: CPC or LTCP. Attaining these operations from a

This is an open access article under the terms of the [Creative Commons Attribution](https://creativecommons.org/licenses/by/4.0/) License, which permits use, distribution and reproduction in any medium, provided the original work is properly cited.

© 2024 The Authors. *IET Microwaves, Antennas & Propagation* published by John Wiley & Sons Ltd on behalf of The Institution of Engineering and Technology.

single structure remains a desirable core objective. For practical applications, a multifunctional converter should not increase the structure and design complexity, size, and thickness. Simultaneously, it must attain critical criteria, such as broad BW, insensitivity to wide incident angles, and high efficiency in polarisation conversions.

To meet these goals, efforts have been made to integrate both CPC and LTCP properties into a single-design assembly [35–40]. Pouyanfar *et al.* introduced a PC incorporating the CPC and LTCP modes. But, this design exhibited limitations such as a narrow BW, lower conversion efficiency, and a relatively large size and thickness compared to the operational wavelength [35]. Various attempts have also been made to improve both BW and efficiency. Designs such as the fish-like structure and a corner-cut square patch showed slight improvements in BW, but they still had large unit-cell sizes, and the efficiency of LTCP remained unexplored [37, 38]. In contrast, a design utilising two meander lines and a cut wire increased the BW for both CPC and LTCP [41], but it suffered from a drop in CPC efficiency below 90%, and the size and thickness increased significantly. Additionally, it only produced one type of circularly polarised wave. Conversely, a recent study achieved high efficiency in generating both left-hand circularly polarised (LHCP) and RHCP waves [42]. However, this accomplishment came at the cost of a substantial decrease in the CPC BW, a large size, and incident angle insensitivity limited to 30°.

In another investigation, an increase in both CPC and LTCP BW was observed, but this improvement was accompanied by a relatively large unit-cell size and thickness. Besides, incident angle insensitivity was restricted to 30°, and the study did not analyse the LTCP type and efficiency [43]. In another recent study, a reduction in unit-cell size and thickness was achieved, resulting in a significant reduction in BW, and the design only produced LHCP waves [44]. Thus, achieving wide BW, high conversion efficiency, the concurrent generation of LHCP and RHCP waves, and ensuring broad angular stability for both the CPC and LTCP polarisations in a single-layer unit-cell with minimised size and thickness are the central properties that remain as the foremost objectives for advancements in PCs.

The proposed metasurface showcases multifunctionality by achieving a wide CPC BW (4.89–8.34 GHz) comparable to other designs of its kind. Simultaneously, its LTCP generates both LHCP (4.55–4.65 GHz) and RHCP (8.54–8.69 GHz) EM waves. These remarkable features result from a novel, single-layer, non-complex, low-profile, and anisotropic design. Also, it achieves a high CPC efficiency of 92% and outstanding LTCP conversion efficiencies, reaching 93% for LHCP and 89% for RHCP. Moreover, the metasurface displays resilience in both polarisation conversions against  $x$ -/ $y$ -polarised waves, and it maintains a stable incident angle performance, extending up to 40° for CPC and 30° for LTCP. The scalability of the proposed unit-cell enhances flexibility, enabling its application across various bands, including mmWave, by adjusting its size up or down. The proposed design comprises a metallic dual-cut SRR, a square patch on top, and a metallic ground spaced by an FR4 substrate layer. The polarisation conversions are demonstrated through a detailed analysis. The performances of the proposed anisotropic

structure have been verified through extensive experiments to produce linear cross-polarisation.

The remainder of this paper is organised as follows. Section 2 focuses on analysing the parameters and designing the unit-cell structure. Section 3 presents the full-wave simulations of the incident angle, polarisation insensitivity, and other figures of merit. Section 4 covers the working principles of the unit-cell and presents reflection parameters and surface currents. Section 5 analyses the geometric parameters and scalability of the proposed unit-cell. Section 6 provides the experimental results and a discussion of the findings. Section 7 concludes the paper by summarising its core outcomes.

## 2 | PERFORMANCE PARAMETERS AND UNIT-CELL DESIGN

In this section, the core parameters of the PC are introduced, which can be used to assess its effectiveness. In the later part of this section, the design stages of the proposed unit-cell are elaborated, involving the evaluation of certain key parameters.

### 2.1 | Performance parameters analysis

When a wave is reflected from an MS, it generates two field components. The first wave has the same polarisation as the incident wave, and it is called the co-polarised reflected field. The other distinct component has a polarisation orthogonal to the incident polarisation, and it is known as the cross-polarised reflected field. These two field components can be controlled by the design of the unit-cell form, allowing the manipulation of the polarisation state of the reflected wave.

The ratio of the reflected field with polarisation  $x$  to the incident field with polarisation  $y$  is given by  $R_{xy}$ , which further measures the proportion of the incident field reflected by a specific polarisation state, which can provide vital information about the performance of the MS as a PC. Also, one way to evaluate the efficiency of a linear PC is to use a polarisation-conversion ratio (PCR). In a case where the incident electric field is polarised along the  $y$ -axis, PCR can be derived using Equation (1) [37]. Similarly, for an incident that is polarised along the  $x$ -axis, the PCR calculation can be adapted by interchanging the  $x$  and  $y$  subscripts in Equation (1).

$$\text{PCR} = \frac{|r_{xy}|^2}{|r_{xy}|^2 + |r_{yy}|^2}. \quad (1)$$

where in Equation (1),  $r_{xy} = |E_{rx}|/|E_{iy}|$  and  $r_{yy} = |E_{ry}|/|E_{iy}|$  are the reflection coefficients for both the cross- and co-polarisation, respectively;  $E$  denotes the electric field of the wave, and  $i$  and  $r$  denote the incident and reflected EM waves, respectively. Comparably, the effectiveness of a circular PC in managing polarisation is measured using the polarisation-maintaining ratio (PMR), as in Equation (2) [45], which indicates the performance of the circular PC in maintaining

the polarisation of a right-hand circularly polarised (RHCP) wave.

$$\text{PMR} = \frac{|r_{rl}|^2}{|r_{lr}|^2 + |r_{rr}|^2}. \quad (2)$$

where  $r$  and  $l$  subscripts represent the RHCP and left-hand circularly polarised (LHCP) states, respectively. For an LHCP wave, the subscripts in Equation (2) above are switched with  $r$  and  $l$  interchanging. The circular polarisation is attained when the magnitudes of the major ( $r_{xy}$ ) and minor ( $r_{yy}$ ) axis components are equal, and the phase difference between them is an odd multiple of  $\pi/2$  [46]. To quantify the level of the circularly polarised wave, the normalised ellipticity ( $e$ ) parameter can be deployed as in Equation (3) for the  $y$ -polarised incident wave [37].

$$e = \frac{2|r_{xy}||r_{yy}|\sin \Delta \varphi}{|r_{xy}|^2 + |r_{yy}|^2}. \quad (3)$$

where in Equation (3)  $\Delta \varphi = \varphi_{yy} - \varphi_{xy}$  is the phase difference between both the co- and cross-polarised reflected fields,  $\varphi_{yy}$  and  $\varphi_{xy}$  represent the reflection phases for co- and cross-polarisation, respectively. When  $r_{xy}$  is equal to  $r_{yy}$  and  $\Delta \varphi = 90^\circ + 2n\pi$  (where  $n$  is an integer), the normalised value of  $e$  is  $+1$ . In this scenario, the reflected wave is LHCP. If the conditions  $r_{xy} = r_{yy}$  and  $\Delta \varphi = -90^\circ + 2n\pi$  are satisfied, then the normalised value of  $e$  is  $-1$ . In this case, the reflected wave is RHCP. In addition, the axial ratio (AR) is a commonly used parameter for determining the degree of circular polarisation of a wave. The AR parameter can be obtained using Equation (4) for both  $x$ - and  $y$ -polarised incident waves [38].

$$\text{AR} = 10 \log \frac{|r_{xy}|}{|r_{yy}|} = 10 \log \sqrt{\frac{1 - \cos \Delta \varphi}{1 + \cos \Delta \varphi}}. \quad (4)$$

In Equation (4), when the magnitudes of  $|r_{xy}|$  and  $|r_{yy}|$  are equal and the phase difference  $\Delta \varphi$  is equal to  $\pm 90^\circ + 2n\pi$ , the AR is 0 dB, indicating a circularly polarised wave. Also, the AR takes on a negative dB value in cases where  $|r_{xy}| < |r_{yy}|$ .

## 2.2 | Unit-cell design

The design of the final unit-cell and its two-dimensional array are shown in Figure 1. The unit-cell building block had a dual-cut (unequal size) SRR and a square patch on its top, with a continuous copper plane at the bottom. A 3.2-mm-thick ( $t_2$ ) FR4 laminate separated the top and bottom layers, with a copper thickness ( $t_1$  and  $t_3$ ) of 0.035 mm. The FR4's relative permittivity and loss tangent are 4.4 and 0.02, respectively. The dimension parameters of the unit-cell were optimised to achieve the desired results and are displayed in Figure 1c as  $p = 10$  mm,  $w_2 = w_1 = w_3 = 1$  mm,  $l_1 = 16$  mm,  $l_2 = 12.5$  mm,  $l_3 = 11$  mm, and  $g = 0.5$  mm.

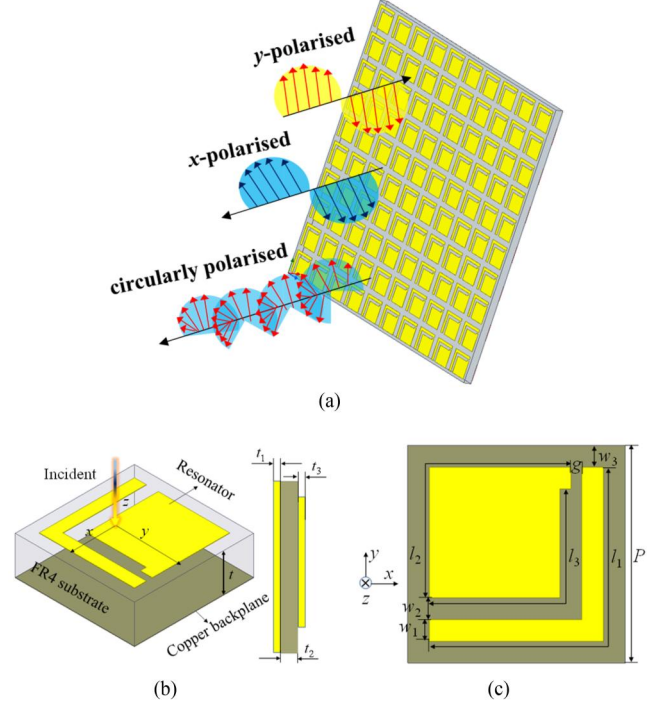


**FIGURE 1** (a) Modelling and simulation of the proposed metasurface PC, (b) perspective view with thickness, and (c) top view of the proposed unit-cell.

The evolution of the proposed metasurface design involves four significant steps in its development. Initially, we selected a well-known metallic SRR on a  $10 \times 10$  mm<sup>2</sup> FR4 substrate grounded in a copper plate. We studied the polarisation of the reflected fields for  $y$ -polarised incidents. The SRR unit-cell at Stage-1, presented in Figure 2a, lacks polarisation conversion ability, as proven by the fact that the cross-polarised reflection coefficient ( $r_{xy}$ ) is 0, but the co-polarised reflection coefficient ( $r_{yy}$ ) is at its peak as shown in Figure 2b. This implies that the unit-cell does not reflect any energy from the cross-polarised wave and reflects the maximum amount of energy from the co-polarised wave. The isotropic nature of the metallic SRR is the cause of the lack of polarisation conversion capability, as well as the high co-polarised reflection coefficient. Also, the isotropic nature results in the designed unit-cell responding equally to both orthogonal components of  $x$ - and  $y$ -polarised incident fields. The orthogonal components are separated into  $+45^\circ$  and  $-45^\circ$  directions along the  $x$ - and  $y$ -axis. As both of these orthogonal elements have a similar form, no phase shift occurs, and the cross-polarised reflection from the orthogonal parts was close to zero, as in Figure 2b.

In Stage-2, two equal size gaps ( $g_1 = g_2 = 1$  mm) were introduced to destroy symmetry. Figure 2c shows the reflection behaviour from this asymmetric shape, observing that  $r_{xy}$  has increased from 0 to 0.96 at 4.88 GHz and 0.76 at 8 GHz. To boost the value of  $r_{xy}$ , at Stage-3, the size of gap  $g_1$  is reduced to 0.5 mm, while the size of gap  $g_2$  remains unchanged. Figure 2d shows that the introduction of unequal size gaps ( $g_1 \neq g_2$ ) increased the value of  $r_{xy}$  to 0.87 at around 7.5 GHz. The final stage of the design involved the addition of an

optimised square patch. The addition led to a marked improvement in the value of  $r_{xy}$ , exceeding 0.9, across frequencies from 4.89 to 8.34 GHz, as shown in Figure 2e. Also, creating high levels of structural capacitance and inductance results in wideband reflection within the C and X bands. The performance of the orthogonal components of a  $y$ -polarised incident wave faced a metallic construct form with both a continuous strip and gap. The  $+45^\circ$  orthogonal component experienced an inductive output owing to the continuous metal strip. On the contrary, the  $-45^\circ$  orthogonal component exhibited capacitive behaviour due to the metallic gap. Similar performance is noted for  $x$ -polarised waves as is observed for  $y$ -polarised waves.

The PCR for equal and unequal size gaps was calculated for the final stage to understand the significance of unequal size gaps. As depicted in Figure 3a, the unequal size gap yielded a CPC efficiency of over 92% across the 4.89–8.34 GHz range. In contrast, the equal size gap slightly widens the BW (by 0.25 MHz) but results in an efficiency reduction to below 92% for a range of 7.23–8.36 GHz, amounting to a small BW increase at the cost of efficiency loss at a considerable BW (1.13 GHz). This trade-off suggests that an unequal size gap configuration is comparatively more efficient. To understand the reflection mechanism, the effective impedance of the proposed structure was determined using the scattering ( $S$ )-parameter retrieval method [47]. The subsequent equation was used to extract the normalised intrinsic impedance of the PC.

$$Z = \pm \sqrt{\frac{(1 + S_{11})^2}{(1 - S_{11})^2}}. \quad (5)$$

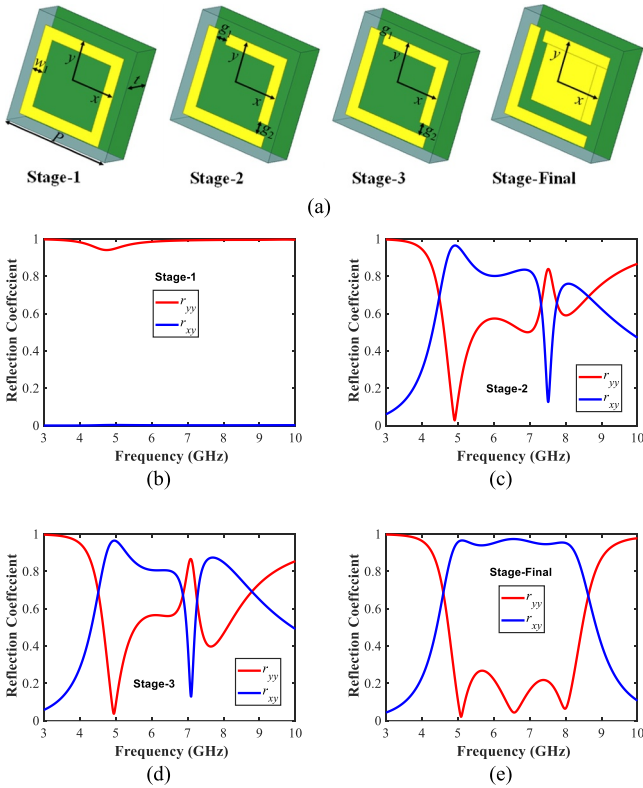
where  $Z$  and  $S_{11}$  are the effective impedance and reflection coefficients, respectively. In Figure 3b, the normalised real and imaginary impedance components are shown. The normalised real impedance consistently hovers near unity throughout the spectrum of 4.89–8.34 GHz. Concurrently, the normalised imaginary part remains close to zero in this range. Notably, in this span, the normalised impedance of the real part aligns effectively with the normalised impedance of free space. This alignment satisfies the impedance matching condition of the PC with the free space, resulting in minimised co-polarised reflection ( $r_{yy}$ ) and maximised cross-polarised reflection ( $r_x$ ) at this frequency range [48] as depicted in Figure 2e. Particularly, below 4.89 GHz and above 8.34 GHz, the normalised real part deviates significantly from the unity value, and thus, high co-polarised reflection occurs.

Table 1 provides additional clarity by demonstrating that the normalised real impedance values align with unity at 5.09, 6.57, and 7.99 GHz. The normalised imaginary components at these frequencies are near zero, and therefore, the co-polarised reflection is noticeably reduced at these specific frequencies.

### 3 | UNIT-CELL SIMULATION RESULTS

The proposed unit-cell structure was simulated in a full-wave mode using Ansys HFSS by deploying periodic boundary (i.e. Master-Slave) conditions along the  $x$ -axis and  $y$ -axis, and the excitation was introduced in the  $z$ -direction.

In Figure 4, the performance of the proposed MS is depicted through its co- and cross-polarised reflection coefficients for the case where a  $y$ -polarised field ( $E_i = \hat{y}E_0e^{jkz}$ ) is incident on the surface at a  $0^\circ$  angle. Figure 4a shows the magnitude of the co- and cross-reflection. Besides, as shown in



**FIGURE 2** (a) Evolution of the proposed unit-cell to attain optimal performance for co- and cross-polarisation reflections, (b) Stage-1, (c) Stage-2, (d) Stage-3, and (e) Stage-Final.

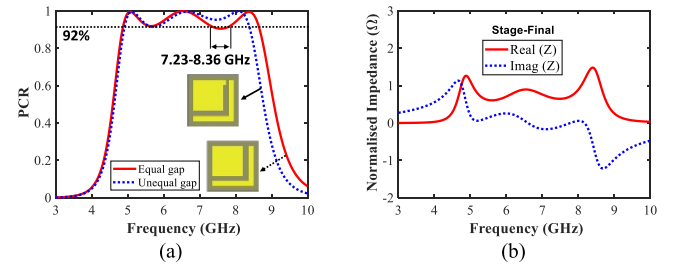


**FIGURE 3** (a) PCR for equal and unequal size gaps at Stage-Final and (b) extracted normalised real and imaginary impedances of the PC.

**TABLE 1** Normalised real and imaginary impedance values.

Frequency (GHz)	Real ( $Z$ )	Imaginary ( $Z$ )
5.09	0.95	0.08
6.57	0.89	0.02
7.99	0.88	0.05

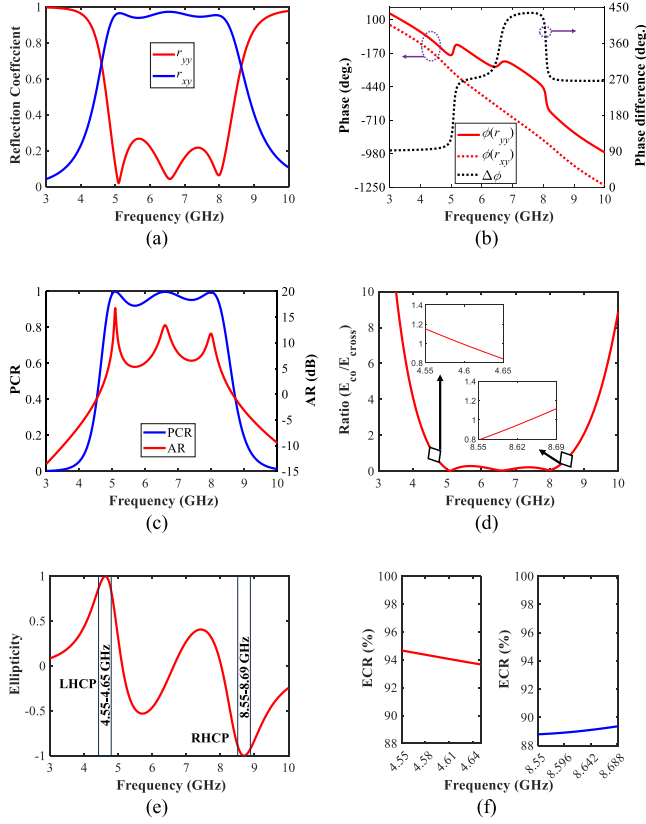


**FIGURE 4** Reflection performances of the proposed PC for  $y$ -polarised waves under normal incidence: (a) co- and cross-reflection magnitudes, (b) phase of both reflections, (c) PCR and AR, (d) co- and cross-polarised reflected field ratios, (e) ellipticity value, and (f) ECR for LHCP (left) and RHCP (right).

Figure 4a, it can be noted that the cross-reflection magnitude exceeds 0.9 for a range of 4.89–8.34 GHz, showing highly efficient cross-polarisation behaviour. The magnitude of the co-polarisation reflection in the same spectrum was also negligible, indicating minimal reflected energy.

The high cross-polarisation conversion efficiency of the MS is shown in Figure 4c, where the PCR beyond 92% between 4.89 and 8.34 GHz is observed. Figure 4c also reveals that the PCR reaches its maximum value of 1 at frequencies of 5, 6.6, and 8 GHz, indicating a peak performance at these frequencies. The phase output shows a major difference ranging from  $+90^\circ$  to  $+430^\circ$  in the 4.89–8.34 GHz range, as depicted in Figure 4b.

Despite this wide variation in phase, the PCR performance is not affected because its calculation is independent of the phase, as indicated by Equation (1). The high PCR performance can be attributed to the magnitude of  $r_{xy}$  being significantly higher than that of  $r_{yy}$  within the range from 4.89 to 8.34 GHz. This range covers both the C and X bands as shown in Figure 4. The PC efficiently works as a high-performance cross-polarisation converter. Figure 4a also shows that at frequencies of 4.62 and 8.69 GHz, the magnitudes of co- and cross-polarisation reflections ( $|r_{yy}| = |r_{xy}| = 0.68$ ) are equal. Figure 4b demonstrates that at the same frequencies, there are phase differences of  $+90^\circ$  and  $+270^\circ$ .

The phases of the reflected EM waves are odd multiples of  $90^\circ$ , while the magnitudes of the co- and cross-polarisation reflections are equal at 4.62 and 8.69 GHz. The characteristics indicate that the proposed design reflects circularly polarised waves when linearly polarised incident waves are applied [49]. As shown in Figure 4c, the designed assembly exhibits an AR of 0 at 4.62 and 8.69 GHz. The BW of a circularly polarised wave can be obtained by the frequency range in which the AR is less than 3 dB [49]. Particularly, a negative AR value was detected beyond the operational frequency range, as indicated in Figure 4c. This negativity arose due to the decrease in the magnitude of the major component ( $|r_{xy}|$ ) relative to the minor component ( $|r_{yy}|$ ) as depicted in Figure 4a.

Furthermore, the ratio between the co-polarised and cross-polarised reflection fields can be evaluated to determine the performance of a circular PC. This ratio should be within the range of  $0.85$ – $1.15$ , and the phase difference between fields should be within the range of  $n90^\circ - 5$  and  $n90^\circ + 5$ , where  $n$  is an odd integer [37]. Moreover, AR is less than 1 dB in the proposed structure over the ranges from 4.55 to 4.65 GHz and 8.55–8.69 GHz, indicating that it can effectively generate circularly polarised waves in these frequency ranges, as shown in Figure 4d. Also, Equation (3) can be used to calculate the ellipticity, and the values obtained indicate the type of circular polarisation produced at different frequencies.

At 4.62 and 8.68 GHz, the  $e$  values are  $+1$  and  $-1$ , indicating LHCP and RHCP, respectively, as in Figure 4e. The energy conversion efficiency of circularly polarised EM waves was assessed by first analysing the PCR. Figure 4c reveals that at frequencies of 4.62 and 8.68 GHz, the PCR is around 0.6. This suggests that over half of the energy was transformed in the orthogonal direction. The energy conversion ratio (ECR) serves as a measure to determine the efficiency of the entire energy conversion process and is defined as Equation (6) [50].

$$\text{ECR} = (|\vec{E}_{rx}|^2 + |\vec{E}_{ry}|^2) / |E_{iy}|^2 = |r_{xy}|^2 + |r_{yy}|^2. \quad (6)$$

where  $E_{rx}$  and  $E_{ry}$  represent the energy reflected in the  $x$ -axis and  $y$ -axis directions, respectively, when an incident wave  $E_{iy}$  propagates along the  $y$ -axis. From Figure 4f, it can be observed that the LHCP conversion efficiency exceeds 93% within the frequency range spanning from 4.55 to 4.65 GHz. Similarly, the RHCP conversion efficiency remained above 89% in the 8.55–8.69 GHz range. These outcomes show a notable attribute of efficiently converting a linearly polarised incident wave into both LHCP and RHCP waves. In real-world scenarios, waves can approach structures from various oblique angles. Hence, ensuring a consistent response, even when facing deviations in the angle of incidence, would significantly broaden the PC's practicality. Given the importance of these attributes, stable incident-angle performance for both transverse electric (TE) and transverse magnetic (TM) polarisations is given below.

### 3.1 | Incident angle and polarisation insensitivity

A PC must exhibit stable performance in practical scenarios irrespective of the wave's incident angle or polarisation mode. The results demonstrated in Figure 5a,c reveal that the PC maintains over 80% CPC performance for incident angles up to 40° within the frequency range of 4.89–8.34 GHz with a steady output observed for both TE and TM modes. Figure 5b, d also show that the PCR performance of the PC remains stable and polarisation insensitive for incident angles of up to 40°. Figure 5a,c depict that despite changes in incident angles and polarisation modes, within the ranges of 4.55–4.65 and 8.55–8.69 GHz, where LTCP is attained, the magnitudes of the co- and cross-polarisation reflections remain the same.

To examine LTCP performance, analysing phase difference and AR behaviour within the ranges of 4.55–4.65 GHz and 8.55–8.69 GHz is essential. As shown in Figure 6a,b, the analysis reveals that the PC can maintain a stable LTCP performance for incident angle variations of up to 30°. Also, the wide incident-angle operation of the PC can be attributed to

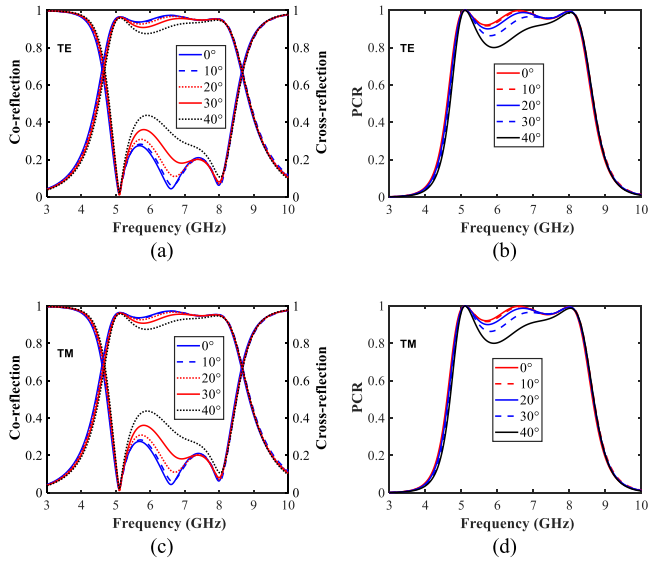


**FIGURE 5** (a) Magnitude of co- and cross-polarisation reflections for TE mode, (b) PCR for TE case, (c) co- and cross-polarisation reflections for TM mode, and (d) PCR for TM case.

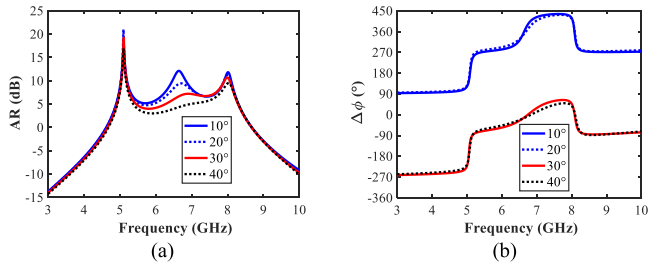


**FIGURE 6** AR, and co- and cross-polarisation phase differences at various incident angles for  $y$ -polarised incident waves: (a) AR and (b) phase difference.

the size of its unit-cell concerning its operating wavelength. The proposed unit-cell has a dielectric thickness of  $0.07\lambda$  and a size of  $0.22\lambda \times 0.22\lambda$  at a centre frequency of 6.6 GHz, which is significantly smaller than the operating wavelength. This is consistent with a study demonstrating that achieving better angular stability is feasible when dimensions are much smaller than the operating wavelength [37]. Thus, the structure shows polarisation insensitivity and stable output operation at a wide incident angle for the CPC and LTCP.

## 4 | WORKING PRINCIPLES

This section presents a comprehensive understanding of the proposed PC by dissecting the  $y$ -polarised incident wave into its  $u$  and  $v$  components, accompanied by an analysis of the surface current distribution, to offer insights into the proposed structure and associated performance parameters.

### 4.1 | Reflection parameters for $u$ - and $v$ -components

An analysis of the  $xy$  and  $uv$  coordinates was conducted to grasp the operational mechanism of the proposed PC. The incident wave, polarised in the  $y$ -direction ( $E_i$ ), is considered along with its two components in the  $u$ - and  $v$ -axes, as shown in Figure 7. The  $u$ - and  $v$ -axes are positioned at angles  $-45^\circ$  and  $+45^\circ$  to the  $y$ -axis, respectively. The incident electric field ( $E_i$ ) and reflected field ( $E_r$ ) can be separated into two mutually perpendicular parts along the  $u$ - and  $v$ -axes, as shown in Figure 7. Equations (7) and (8) can be used to denote the incident and reflected waves, respectively.

$$E_i = \hat{y}E_i = \hat{u}E_{iu} + \hat{v}E_{iv}. \quad (7)$$

$$E_r = \hat{u}E_{ru} + \hat{v}E_{rv} = \hat{u}r_uE_{iu} + \hat{v}r_vE_{iv}. \quad (8)$$

where  $\hat{u}$  and  $\hat{v}$  are the unit vectors, and  $r_u$  and  $r_v$  denote the complex reflection coefficients along the  $u$ - and  $v$ -axes. The expression for the reflected wave is given by Equation (9) [37].

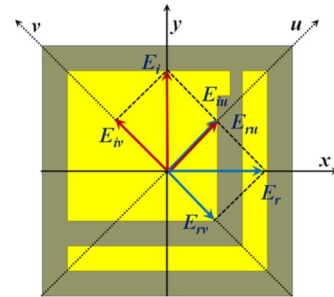


**FIGURE 7** Core structure, parameters, and working principles of the proposed multifunctional unit-cell for the purpose of polarisation conversions.

$$E_r = \hat{u} (r_{uu} E_{iu} e^{i\varphi_{uu}} + r_{uv} E_{iv} e^{i\varphi_{uv}}) + \hat{v} (r_{vv} E_{iv} e^{i\varphi_{vv}} + r_{vu} E_{iu} e^{i\varphi_{vu}}). \quad (9)$$

where  $r_{uu}$ ,  $r_{vv}$ , and  $r_{uv}$ ,  $r_{vu}$ , represent the magnitudes of the co- and cross-polarisation reflections, respectively. Additionally,  $\varphi_{uu}$ ,  $\varphi_{uv}$ , and  $\varphi_{vv}$ ,  $\varphi_{vu}$ , as phase parameters denote the co- and cross-phases along the  $u$ - and  $v$ -axes, respectively.

Owing to its asymmetric shape, the PC exhibits anisotropy with inhomogeneous permittivity and permeability [51]. Thus, the phases and magnitudes of the reflected waves can differ. As shown in Figure 7, the resultant reflected field for  $u$ - and  $v$ -polarised waves is along the  $x$ -axis if  $r_{uu} = r_{vv} \approx 1$ ,  $r_{uv} = r_{vu} \approx 0$ , and  $\Delta\varphi = \varphi_{uu} - \varphi_{vv} = \pm 180^\circ + 2k\pi$ , where  $k$  is an integer. This suggests that  $u$ - and  $v$ -polarised waves undergo a  $90^\circ$  rotation during reflection, exhibiting CPC output. In contrast, the LTCP occurs when  $\Delta\varphi = \varphi_{uu} - \varphi_{vv} = \pm 90^\circ + 2k\pi$ , where  $k$  is an integer [37].

To validate the evaluation, a simulation of the proposed PC was conducted to investigate the magnitude of the reflection coefficient and reflection phase for  $u$ - and  $v$ -components. Figure 8a,c present the reflection coefficient magnitudes for normal and  $40^\circ$  incident angles, revealing that cross-polarised reflection is negligible throughout the desired range, while co-polarised reflection approaches unity. However, this analysis alone cannot confirm CPC and LTCP conversion bands, and further analysis is needed to assess the polarisation conversion range. Thus, Figure 8b,d show the phase difference for  $0^\circ$  and  $40^\circ$  incidents that fall in the range of approximately  $-180^\circ$  to  $+180^\circ$  for the bands between 4.89 and 8.34 GHz, validating linear cross-polarisation reflection across this broad spectrum. The phase difference between frequencies of 4.55–4.65 GHz and 8.55–8.69 GHz is almost  $\pm 90^\circ$  or  $\pm 270^\circ$ , indicating the presence of LTCP behaviour.

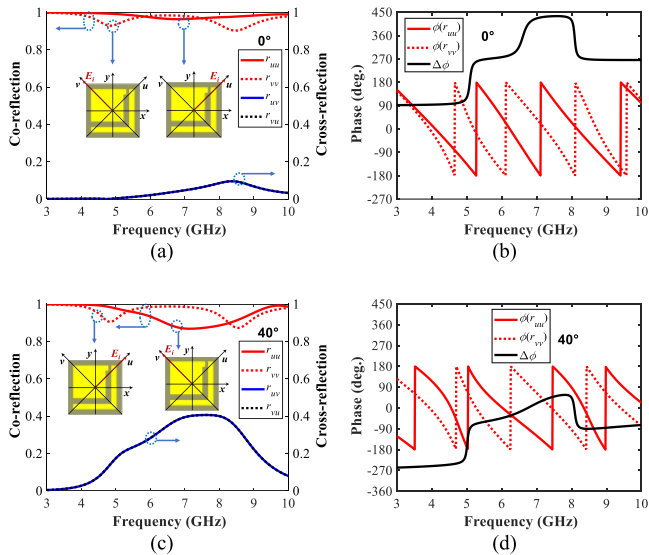


**FIGURE 8** Reflection parameters for  $u$ - and  $v$ -components: (a) the magnitude of reflection coefficients at normal incidence, (b) phase difference at normal incidence, (c) the magnitude of reflection coefficient at  $40^\circ$  incidence, and (d) phase difference at  $40^\circ$  incidence.

## 4.2 | Surface current analysis

The peak PCR values for PC were observed at 5, 6.6, and 8 GHz. These three resonances were considered to provide a better understanding of the principles of PC by describing the corresponding current distribution. Figure 9 shows the presence of an anti-parallel current on the top and bottom layers of the unit-cell for both  $u$ - and  $v$ -components. This leads to a loop current flowing in the dielectric layer, constructing magnetic resonance. According to a study, the optimal efficiency is due to the conflation of PCRs at and close to the resonances [52].

## 5 | GEOMETRIC PARAMETER ANALYSIS

The geometric parameters of a PC play an essential role in determining its performance characteristics. These parameters include size, configuration, orientation, and spacing as part of the unit-cell design. Additionally, parametric analysis assists in fixing the final optimised structure, as shown in Figure 1.

To determine the optimal periodicity of the developed PC, parameter  $P$  varied from 9 to 11 mm in increments of 0.5 mm, while holding other parameters constant. The results in

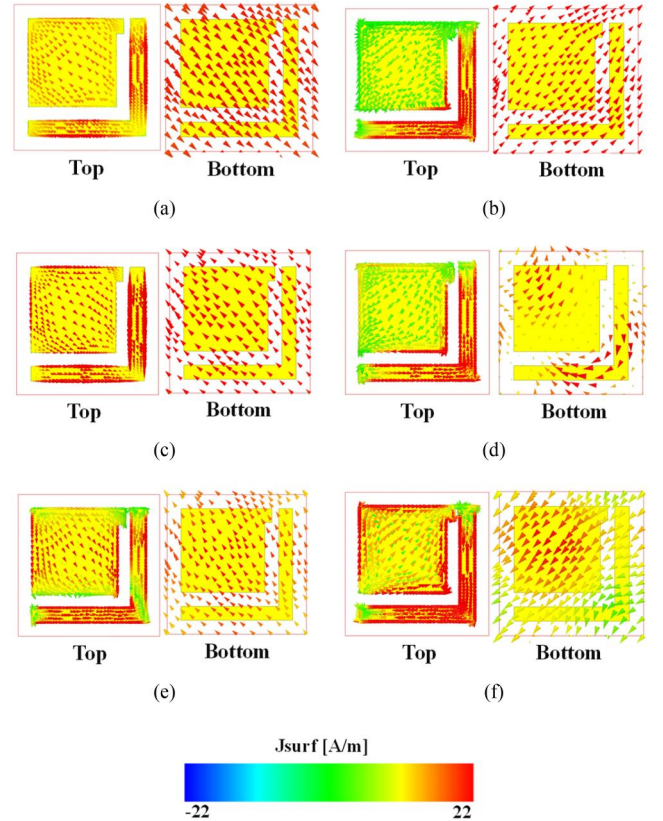


**FIGURE 9** Surface current distribution on the top and bottom layers of the unit-cell for normal incidence at the resonance frequencies: (a, b)  $u$ -component and  $v$ -component at 5 GHz, (c, d)  $u$ -component and  $v$ -component at 6.6 GHz, (e, f)  $u$ -component and  $v$ -component at 8 GHz.



Figure 10a show that the proposed PC with a  $p$  value of 10 mm maintains a PCR of more than 92% within the frequency range of 4.89–8.34 GHz. Nonetheless, lowering the  $p$  value to 9 mm causes a substantial decrease in the PCR operation near 7.8 GHz, while increasing it to 11 mm reduces the BW and weakens the PCR rate at approximately 6 GHz.

Using other values for  $P$  resulted in either decreased PCR or reduced BW. The  $p$  value was 10 mm as it provided optimal PCR and BW performance. Also, once the  $p$  value is finalised, the gap  $g$  is varied in simulation from 0.5 to 0.2 mm with a step size of 0.1 mm decrement. The importance of retaining the value of  $g$  (0.5 mm) is discussed in the PC evolution. Thus, only the effect of decreasing  $g$  from 0.5 mm is considered in this analysis. According to Figure 10b, decreasing the value of  $g$  can sustain a PCR of more than 92%. However, there was a decrease in BW as the value of  $g$  decreased. Hence, the value of  $g$  is set to 0.5 mm since it has been verified that this value provides optimal performance for both the widest BW and the highest PCR. Another gap ( $w_2$ ) is adjusted from 0.6 to 1.4 mm in increments of 0.2 mm, while  $P$  and  $g$  are also kept at their optimised values.

According to the results in Figure 10c, optimal performance was achieved when  $w_2$  was set to 1 mm. However, reducing  $w_2$  to 0.6 mm increases BW while causing a decline in the PCR performance at around 5.8 GHz. On the contrary,

increasing  $w_2$  to 1.4 mm decreases BW and lowers PCR performance at around 7 GHz. Moreover, in simulations, the dielectric layer's thickness ( $t$ ) varies from 2.8 to 3.6 mm in 0.2 mm increments, with other parameters being constant. Figure 10d presents that increasing the thickness results in a performance shift towards lower frequency ranges while decreasing it leads to a change near higher frequencies. However, setting  $t$  to 3.2 mm yields the desired PCR and BW. Another essential parameter patch dimension ( $l_x$  and  $l_y$ ) varied from 4.5 to 5.5 mm with 0.5 mm step size. Figure 10e shows the PCR performance for different patch sizes. Notably, when  $l_x = l_y = 5$  mm, the PCR maintained optimal efficiency and BW. Still, an increase in the patch size results in a reduction in BW and efficiency. Conversely, a decrease in patch size leads to an increase in BW but comes at the cost of a major reduction in efficiency. To understand the effect of substrate loss, the PCR was calculated for various loss tangents of the FR4 substrate. Figure 10f shows that the loss tangent has a minor effect on PCR performance.

The proposed unit-cell structure performs well in the 4.89–8.34 GHz range. However, the structure was scaled from 0.75 to 1.75 in the XY plane to investigate its potential applications in other ranges. Figure 11a,b shows that scaling the structure to 0.75 shifts the LTCP operation frequency from 4.62 and 8.69 GHz to 5.58 and 10.96 GHz, respectively. The working frequency for CPC shifts from 4.89–8.34 GHz to

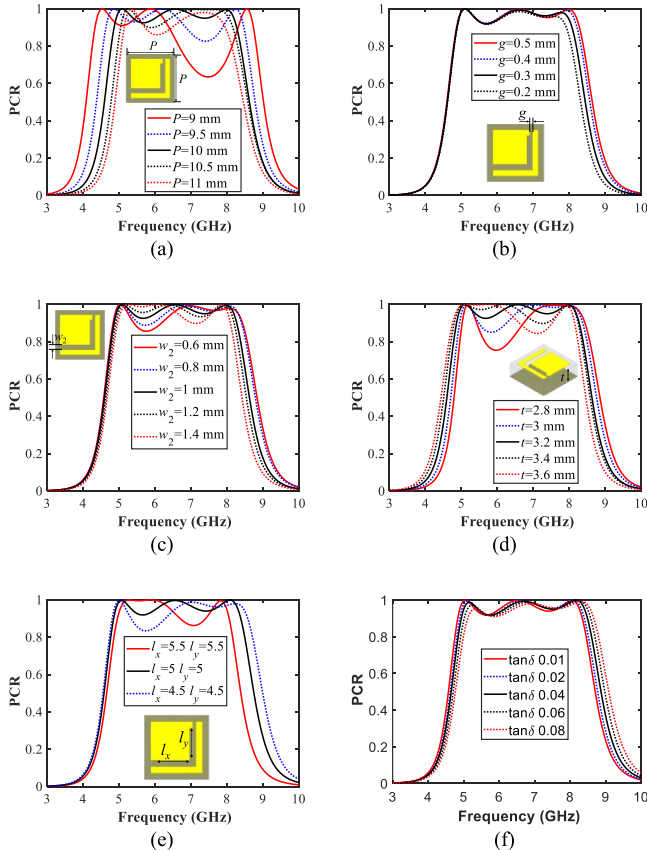


**FIGURE 10** Simulated and numerical PCR variations of the PC for different parameters: (a)  $p$ , (b)  $g$ , (c)  $w_2$ , (d) thickness  $t$ , (e) patch size, and (f)  $\tan\delta$ .

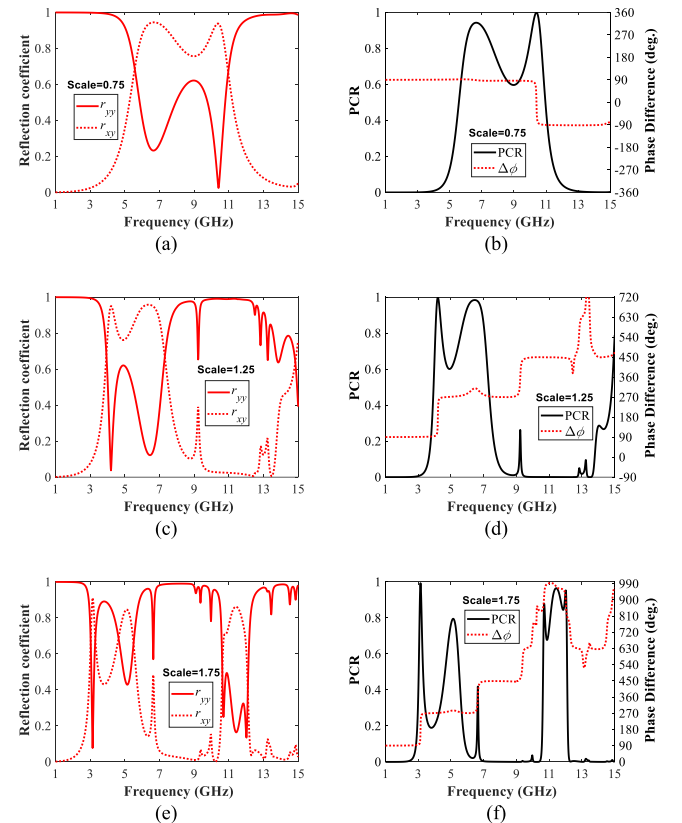


**FIGURE 11** Magnitude of co- and cross-polarisation, PCR, and phase difference of the proposed PC for different scaling of physical dimensions in the XY plane: (a, b) 0.75, (c, d) 1.25, and (e, f) 1.75.

6.22–7.18 GHz and 10.12–10.63 GHz. Similarly, scaling the unit to 1.25 generates LTCP at 3.95 and 7.3 GHz, and CPC occurs in the range of 5.86–6.92 GHz, as in Figure 11c,d. Further scaling to 1.75 generates CP at 3, 3.3, 4.64, and 5.52 GHz, and CPC attains a frequency range of 11.19–11.69 GHz, see Figure 11e,f. Hence, further optimisation of the scaling of the proposed unit may allow the attainment of LTCP and CPC in very high or low-frequency ranges.

Figure 11 depicts that the polarisation conversion performance of the proposed PC can be shifted to either higher or lower frequencies. However, BW and efficiency declined during this frequency shift compared with the original output. Achieving a wide BW and high-efficiency shift requires optimising the scaling and configuration of the top resonator. In Figure 12, the parameters of the original PC configuration are presented.

At first, this configuration was scaled up by a factor of 1.25, and then the lengths of the square patch ( $l_x$  and  $l_y$ ) and gap  $g_2$  are optimised as shown in Figure 12b. The optimisation of the square patch dimensions ( $l_x = l_y = 7.375$  mm) and gap ( $g_2 = 0.125$  mm) leads to a shift in the PCR BW from the original 4.89–8.34 GHz to 4.27–6.34 GHz, achieving an efficiency of over 90%. Notably, this optimised BW remained wide and at a lower frequency. This optimised result further validates how adjusting the resonator assembly, in conjunction with scaling, can effectively shift the BW to a lower frequency.

The lower frequency shift can be elucidated by applying the resonance equation [53],  $f_r = 1/2\pi\sqrt{LC}$ , where  $f_r$  represents the resonance frequency, and  $L$  and  $C$  denote the inductance and capacitance, respectively. Scaling the proposed assembly to 1.25 increases both  $L$  and  $C$  for the PC, leading to a shift in the resonance to a lower frequency according to the resonance equation. This shifted BW is widened and made efficient by fine-tuning the top resonator structure.

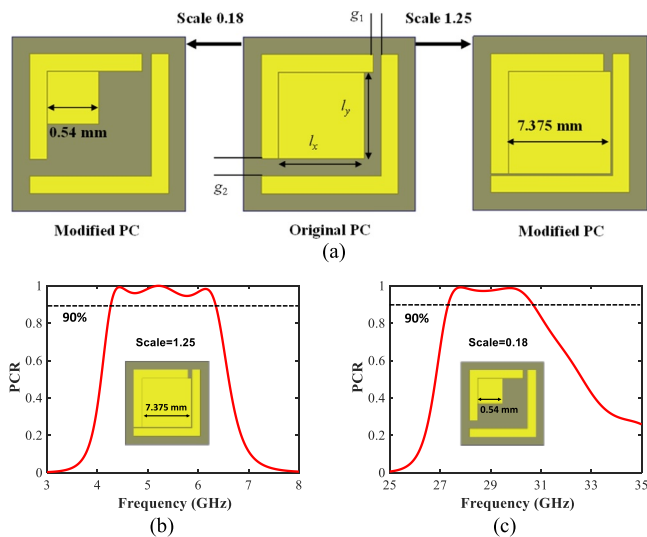


**FIGURE 12** (a) Geometric parameters of the proposed and modified PC, and PCR performance of the modified PC for the optimisation of the top resonator at scaling: (b) 1.25, and (c) 0.18.

The proposed unit-cell was further scaled down to 0.18, and the PCR performance was evaluated to shift the original wide band to a higher frequency. As depicted in Figure 12c, using a scale of 0.18 and optimising the square patch ( $l_x = l_y = 0.54$  mm) resulted in a notable shift of the BW from the original 4.89–8.34 = 3.45 GHz to 27.33–30.68 = 3.35 GHz, achieving over 90% conversion efficiency. This successful near-equal BW shift to mmWave frequencies shows the importance of precise scaling, tuning, and optimisation, and the possibility of shifting the entire BW to other frequencies. Also, the higher frequency shift can be elaborated using the above resonance equation: Lowering the scale reduces both inductance and capacitance. Thus, the resonance of PC shifted to a higher frequency, and subsequently, a wide BW and high efficiency were achieved by optimising the size of the square patch.

## 6 | FABRICATION AND EXPERIMENTAL RESULTS

The proposed PC was fabricated on an FR4 substrate using a  $30 \times 30$  unit-cell arrangement. Figure 13a shows the realised PC, which is  $300 \times 300$  mm<sup>2</sup>; the top and bottom layers are conductive using copper. Figure 13b shows the deployed setup for measuring and testing the developed surface. A Keysight programmable vector network analyser (8361C PNA) and two standard gain horn antennas, as transmitter, Tx, and receiver, Rx, were used to measure the relative reflection characteristics against a solid conductor of exact dimensions.

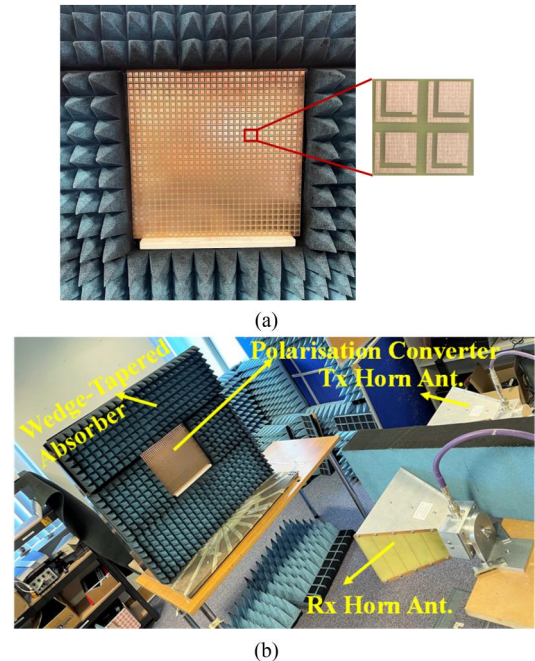


**FIGURE 13** (a) Fabricated PC prototype with the proposed unit-cell as its core building block, and (b) RF measurement setup and its associated equipment, including two DRH-118 wideband horn antennas for normal incident testing, RF, radio frequency.

To eliminate unwanted reflection from the room, the time grating option was enabled in the PNA, where a small time window was created around the maximum reflected power initially measured from the conductor used as a reference. This stage was conducted to validate and experimentally confirm the wideband performance of the PC. The Tx horn emits  $x$ - or  $y$ -polarised waves, and the Rx horn antenna receives  $x$ - and  $y$ -polarised waves. The co- and cross-polarisation reflections were then measured using PNA. Figure 14 shows the measured and full-wave simulated reflection coefficients, PCR, and AR for  $y$ -polarised waves under normal incidence. In this regard, good agreement was observed in the reflection coefficients, PCR, and AR. Figure 14b shows the measured PCR of over 99% for a BW of 4.46–8 GHz.

A non-ideal testing environment and non-linearities of the selected substrate may have caused a slight mismatch between the full-wave simulations (an infinite array was considered) and measurements [37]. The proposed structure's performance at oblique angles could not be measured due to the limitations of the measurement setup and RF equipment.

In order to enable a thorough comparison, researchers have introduced the concept of cost-efficient BW, abbreviated as  $BW_{CE}$ , defined by the expression given as Equation (10) [38]:

$$BW_{CE} = \frac{RBW}{R_v}. \quad (10)$$

where RBW is the relative bandwidth, and  $R_v$  is the relative volume of a unit-cell.  $R_v$  can be expressed as  $T_v/\lambda^3$ , where  $T_v$  is the total unit-cell volume, and  $\lambda$  is the centre frequency within the operational BW of the developed PC.

Finally, Table 2 provides a qualitative comparison between the proposed PC and the current state-of-the-art PCs, mainly regarding their functionalities, unit-cell size, thickness, RBW,  $BW_{CE}$ , PCR, circular polarisation type, operating frequency, polarisation conversion efficiency, and oblique incident angle output.

Conventional PCs are typically single-functional and can generate either CPC or LTCP [10, 20, 21, 25, 27, 29, 32, 51]. By contrast, our proposed PC is multifunctional, simultaneously producing both CPC and LTCP. Notably, most multifunctional PCs operate at higher frequencies, such as the X-band or above [35, 37, 38, 43, 44], with only a few achieving limited performance in the lower C-band. However, these merits often come at

the cost of a lower CPC efficiency [41] or reduced CPC BW [42]. In contrast, our design covers nearly the entire C-band and part of the X-band, delivering both a wide CPC BW and high efficiency. It is essential to highlight that our design features the smallest size ( $0.22\lambda \times 0.22\lambda$ ) among all multifunctional PCs in the comparison table. The unit-cell had a comparable thickness of  $0.06\lambda$ . When assessing the relative BW, our design excels with the highest CPC RBW compared to other reported PCs [35, 37, 38, 44]. While other works, [41, 43], exhibit slightly larger CPC BW, ours is superior in size and polarisation conversion.

Furthermore, our PC offers the broadest cost-effective CPC BW among other multifunctional PCs. When considering the LTCP performance, our design showed comparable RBW and cost-effective BW. Notably, our structure depicts comparable incident angle stability for both CPC and LTCP scenarios.

To delve deeper into our design's superiority, we evaluated the LTCP efficiency and type. While other multifunctional PCs generate either RHCP or LHCP waves [37, 41, 44], our structure stands out by producing both types of circularly polarised waves. Other studies achieved LHCP and RHCP generation [35, 42], with our RHCP efficiency comparable to theirs. But, the comparison shows that our LHCP efficiency outperforms that of other multifunctional PCs.

As observed, our proposed and experimentally tested PC mostly outperformed existing structures regarding several vital aspects and output figures of merit. The proposed PC stands out with its compact size, cost-effective CPC BW, polarisation conversion efficiency, versatility, simple configuration, single-layer assembly, and other core electrical properties, such as wideband output and broad angular stability in both cross and circular polarisation conversions.

## 7 | CONCLUSION

In this study, the design and EM performance evaluation of a polarisation converter (PC) metasurface based on a compact ( $0.22\lambda \times 0.22\lambda$ ), novel, and non-complex unit-cell (as its core building block) were thoroughly investigated. The proposed structure exhibits a single broad cross-polarisation conversion and dual-band linear-to-circular polarisation conversion in the C and partial X bands. Both forms were converted using an anisotropic unit-cell, involving a dual-cut SRR and a square patch. Owing to the anisotropic nature of the assembly, the developed metasurface can achieve efficient cross-polarisation conversion over a range of 4.89–8.34 GHz, with a conversion efficiency exceeding 92%. Even with variations in incident angles up to  $40^\circ$ , efficiency can be attained at or above 80%. The proposed MS demonstrates sustained LTCP conversion at frequencies between 4.55–4.65 and 8.54–8.69 GHz and can further maintain incident angle stability up to  $30^\circ$ . The LTCP performance exhibits its ability to generate LHCP and RHCP, achieving efficiencies exceeding 93% and 89%, respectively.

Moreover, the MS demonstrates equivalent efficiencies for TE and TM waves, implying that polarisation changes do not affect it. A prototype was fabricated and evaluated to verify the accuracy of the full-wave EM simulations, and our results

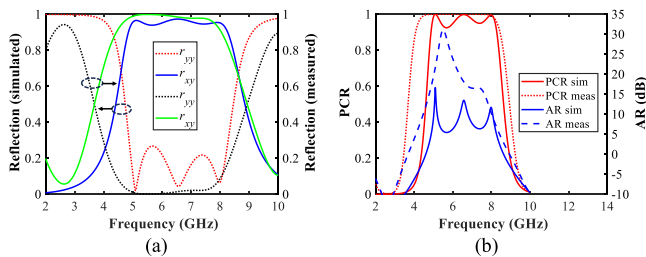


**FIGURE 14** (a) Magnitude of simulated and measured co- and cross-polarisation reflection coefficients. (b) PCR and AR of the PC under normal incidents.

TABLE 2 Comparison of the proposed PC metasurface with related works in microwave frequencies.

Ref.	BW (GHz)	PC type	Multi-functional (Yes/No)	RBW with PCR > 90%	Angular stability (°) > 80%	BW <sub>CE</sub>	Unit-cell size (λ)	Thickness (λ)	Efficiency (%)	Circular polarisation (CP) type
[21]	6.1–19.8	LTCP	No	105.9	NR	28.12	0.34λ × 0.34λ	0.32λ	99.6	Only RHCP
[10]	10.21–22.71	LTCP	No	84	48	68	0.31λ × 0.31λ	0.15λ	83.9	Only LHCP
[32]	10.73–16.13	LTCP	No	40.2	45	17.25	0.4λ × 0.4λ	0.07λ	NR	Only LHCP
[49]	4.7–21.7	LTCP	No	128.7	20	26.64	0.39λ × 0.39λ	0.31λ	NA	Both LHCP & RHCP
[25]	2–8.45	CPC	No	123.4	15	47.46	0.38λ × 0.38λ	0.20λ	90	NA
[27]	8.9–11.1	CPC	No	22	30	143	0.19λ × 0.19λ	0.04λ	99	NA
[20]	12.4–27.96	CPC	No	77	30	38	0.43λ × 0.43λ	0.11λ	90	NA
[29]	13–26	CPC	No	66.66	30	31	0.45λ × 0.45λ	0.10λ	90	NA
[35]	15.5–16.5	CPC	Yes	6.25	60	5.7	0.32λ × 0.32λ	0.11λ	80	NA
	13, 18	LTCP		NR	NR	NR			NR	Both LHCP & RHCP
[37]	8–11	CPC	Yes	31.6	45	130.58	0.26λ × 0.26λ	0.06λ	95	NA
	7.5–7.7 & 11.5–11.9	LTCP		2.6, 3.4	45	10.7, 14.05			NR	Only RHCP
[38]	8–12	CPC	Yes	40	45	142.67	0.23λ × 0.23λ	0.05λ	90	NA
	7.42–7.6 & 13–13.56	LTCP		2.4, 4.2	30	8.6, 14.9			NR	NR
[41]	6.53–12.07	CPC	Yes	59.6 < 90%	NR	98.19	0.29λ × 0.29λ	0.11λ	88	NA
	13.70–15.60	LTCP		13	NR	5.47			89	Only RHCP
[42]	6.46–6.78, 10.52–11.85 & 16.49–17.37	CPC	Yes	4.8, 11.89 & 5.19	30	9.17, 22.72 & 9.91	0.29λ × 0.29λ	0.06λ	90	NA
	7.28–9.40 & 13.38–15.19	LTCP		25.41, 12.67	NR	48.55, 24.21			LHCP > 89, RHCP > 89	Both LHCP & RHCP
[43]	7.74–14.44	CPC	Yes	60.41	30	49.1	0.33λ × 0.33λ	0.11λ	90	NA
	14.95–17.35	LTCP		14.86	30	3.91			NR	NR
[44]	9–12	CPC	Yes	28.57	60	113.09	0.24λ × 0.24λ	0.04λ	90	NA
	8.44–8.58 & 12.74–13.14	LTCP		1.3, 3.8	NR	5.1, 15.04			NR	Only LHCP
<b>This work</b>	<b>4.89–8.34</b>	<b>CPC</b>	<b>Yes</b>	<b>52.3</b>	<b>40</b>	<b>152.94</b>	<b>0.22λ × 0.22λ</b>	<b>0.06λ</b>	<b>92</b>	<b>NA</b>
	<b>4.55–4.65 &amp; 8.54–8.69</b>	<b>LTCP</b>		<b>2.2, 1.7</b>	<b>30</b>	<b>6.3, 5.11</b>			<b>LHCP &gt; 93, RHCP &gt; 89</b>	<b>Both LHCP &amp; RHCP</b>

Abbreviations: NA, not applicable; NR, not reported.

exhibited reasonable consistency. The proposed design shows improved performance in terms of BW, cost-effectiveness, and design intricacy. Finally, the developed MS can potentially be applied for polarisation management in various applications, such as polarisation RF beam splitters, wave plates, antennas, satellite, and radar subsystems, and can be scaled up or down for deployment in other bands. In the future, a potential target can be to investigate the robustness of the realised metasurface and its associated building blocks to determine the absorption characteristics and other related propagation applications.

## AUTHOR CONTRIBUTIONS

**Kd. M. Raziul Islam:** Conceptualisation; Data curation; Formal analysis; Investigation; Methodology; Software; Validation; Visualisation; Writing – original draft; Writing – review & editing. **Ardavan Rahimian:** Conceptualisation; Data curation; Formal analysis; Funding acquisition; Investigation; Methodology; Project administration; Resources; Software; Supervision; Validation; Visualisation; Writing – original draft; Writing – review & editing. **Gabriel G. Machado:** Formal analysis; Investigation; Methodology; Resources; Validation; Writing – review & editing. **Muhammad Ali Babar Abbasi:** Formal analysis; Investigation; Methodology; Resources; Validation; Writing – review & editing. **Adnan Ahmad Cheema:** Formal analysis; Investigation; Methodology; Resources; Supervision; Validation; Writing – review & editing. **Brian J. Meenan:** Formal analysis; Investigation; Methodology; Resources; Supervision; Validation; Writing – review & editing.

## CONFLICT OF INTEREST STATEMENT

No conflict of interest has been declared by the authors.

## DATA AVAILABILITY STATEMENT

The data supporting the findings of this study are available from the corresponding author upon reasonable request.

## ORCID

*Ardavan Rahimian*  <https://orcid.org/0000-0001-9643-3019>

*Gabriel G. Machado*  <https://orcid.org/0000-0001-7663-9044>

*Muhammad Ali Babar Abbasi*  <https://orcid.org/0000-0002-1283-4614>

*Adnan Ahmad Cheema*  <https://orcid.org/0000-0002-2338-6247>

## REFERENCES

- Beruete, M., et al.: Polarisation selection with stacked hole array metamaterial. *J. Appl. Phys.* 103(5), 1–4 (2008)
- Su, P., et al.: An ultra-wideband and polarisation-independent metasurface for RCS reduction. *Sci. Rep.* 6(1), 20387 (2016). <https://doi.org/10.1038/srep20387>
- Liu, Y., et al.: Wideband RCS reduction of a slot array antenna using polarisation conversion metasurfaces. *IEEE Trans. Antennas Propag.* 64(1), 326–331 (2016). <https://doi.org/10.1109/tap.2015.2497352>
- Wu, Z., et al.: Metasurface superstrate antenna with wideband circular polarisation for satellite communication application. *IEEE Antennas Wirel. Propag. Lett.* 15, 374–377 (2016). <https://doi.org/10.1109/lawp.2015.2446505>
- Meissner, T., Wentz, F.J.: Polarisation rotation and the third Stokes parameter: the effects of spacecraft attitude and Faraday rotation. *IEEE Trans. Geosci. Remote Sens.* 44(3), 506–515 (2006). <https://doi.org/10.1109/tgrs.2005.858413>
- Young, L., Robinson, L., Hacking, C.: Meander-line polariser. *IEEE Trans. Antennas Propag.* 21(3), 376–378 (1973). <https://doi.org/10.1109/tap.1973.1140503>
- Huang, Y., Zhou, Y., Wu, S.-T.: Broadband circular polariser using stacked chiral polymer films. *Opt. Exp.* 15(10), 6414–6419 (2007). <https://doi.org/10.1364/oe.15.006414>
- Hao, J., et al.: Manipulating electromagnetic wave polarisations by anisotropic metamaterials. *Phys. Rev. Lett.* 99(6), 063908 (2007). <https://doi.org/10.1103/physrevlett.99.063908>
- Dutta, R., Mitra, D., Ghosh, J.: Dual-band multifunctional metasurface for absorption and polarisation conversion. *Int. J. RF Microw. Comp. Aided Eng.* 30(7) (2020). <https://doi.org/10.1002/mmce.22200>
- Ran, Y., et al.: Ultra-wideband linear-to-circular polarisation converter with ellipse-shaped metasurfaces. *Opt Commun.* 451, 124–128 (2019). <https://doi.org/10.1016/j.optcom.2019.06.049>
- Khan, M.I., Tahir, F.A.: An angularly stable dual-broadband anisotropic cross polarisation conversion metasurface. *J. Appl. Phys.* 122(5) (2017). <https://doi.org/10.1063/1.4997456>
- Khan, M.I., Tahir, F.A.: Simultaneous quarter-wave plate and half-mirror operation through a highly flexible single layer anisotropic metasurface. *Sci. Rep.* 7(1), 16059 (2017). <https://doi.org/10.1038/s41598-017-15279-8>
- Zhang, L., et al.: Ultrabroadband design for linear polarization conversion and asymmetric transmission crossing X- and K- band. *Sci. Rep.* 6(1), 33826 (2016). <https://doi.org/10.1038/srep33826>
- Wu, X., et al.: Anisotropic metasurface with near-unity circular polarisation conversion. *Appl. Phys. Lett.* 108(18) (2016). <https://doi.org/10.1063/1.4948594>
- Khan, M.I., Fraz, Q., Tahir, F.A.: Ultra-wideband cross polarisation conversion metasurface insensitive to incidence angle. *J. Appl. Phys.* 121(4) (2017). <https://doi.org/10.1063/1.4974849>
- Khan, M.I., Tahir, F.A.: A broadband cross-polarisation conversion anisotropic metasurface based on multiple plasmon resonances. *Chin. Phys. B* 27(1), 014101 (2018). <https://doi.org/10.1088/1674-1056/27/1/014101>
- Dutta, R., et al.: Multi-band multifunctional metasurface-based reflective polarisation converter for linear and circular polarisations. *IEEE Access* 9, 152738–152748 (2021). <https://doi.org/10.1109/access.2021.3128190>
- Baghel, A.K., Kulkarni, S.S., Nayak, S.K.: Linear-to-cross-polarisation transmission converter using ultrathin and smaller Periodicity Metasurface. *IEEE Antennas Wirel. Propag. Lett.* 18(7), 1433–1437 (2019). <https://doi.org/10.1109/lawp.2019.2919423>
- Liu, X., et al.: Three-band polarisation converter based on reflective metasurface. *IEEE Antennas Wirel. Propag. Lett.* 16, 924–927 (2017). <https://doi.org/10.1109/lawp.2016.2614686>
- Gao, X., et al.: Ultrawideband and high-efficiency linear polarisation converter based on double V-shaped metasurface. *IEEE Trans. Antennas Propag.* 63(8), 3522–3530 (2015). <https://doi.org/10.1109/tap.2015.2434392>
- Lin, B., et al.: An ultra-wideband reflective linear-to-circular polarisation converter based on anisotropic metasurface. *IEEE Access* 8, 82732–82740 (2020). <https://doi.org/10.1109/access.2020.2988058>
- Fu, C., et al.: Dual-bandwidth linear polarisation converter based on anisotropic metasurface. *IEEE Photon. J.* 12(2), 1–11 (2020). <https://doi.org/10.1109/jphot.2019.2962336>
- Liu, Y., et al.: Dual-band and high-efficiency polarisation converter based on metasurfaces at microwave frequencies. *Appl. Phys. B* 122(6), 178 (2016). <https://doi.org/10.1007/s00340-016-6454-4>
- Lin, B., et al.: Dual-band high-efficiency polarisation converter using an anisotropic metasurface. *J. Appl. Phys.* 119(18) (2016). <https://doi.org/10.1063/1.4948957>

25. Nguyen, T.M., et al.: Ultra-wideband and lightweight electromagnetic polarisation converter based on multiresonant metasurface. *IEEE Access* 10, 92097–92104 (2022). <https://doi.org/10.1109/access.2022.3202530>
26. Kamal, B., et al.: Design and experimental analysis of dual-band polarisation converting metasurface. *IEEE Antennas Wirel. Propag. Lett.* 20(8), 1409–1413 (2021). <https://doi.org/10.1109/lawp.2021.3083334>
27. Lončar, J., Grbic, A., Hrabar, S.: A reflective polarisation converting metasurface at X-band frequencies. *IEEE Trans. Antennas Propag.* 66(6), 3213–3218 (2018). <https://doi.org/10.1109/tap.2018.2816784>
28. Jia, Y., et al.: A dual-patch polarisation rotation reflective surface and its application to ultra-wideband RCS reduction. *IEEE Trans. Antennas Propag.* 65(6), 3291–3295 (2017). <https://doi.org/10.1109/tap.2017.2694879>
29. Ahmad, T., et al.: Ultrawideband cross-polarisation converter using anisotropic reflective metasurface. *Electron* 11(3), 487 (2022). <https://doi.org/10.3390/electronics11030487>
30. Yang, Z., et al.: A broad-band wide-angle linear-to-circular polarisation converter based on stripline metasurface. *IEEE Access* 9, 163204–163213 (2021). <https://doi.org/10.1109/access.2021.3134064>
31. Wang, H.B., Cheng, Y.J., Chen, Z.N.: Dual-band miniaturised linear-to-circular metasurface polarisation converter with wideband and wide-angle axial ratio. *IEEE Trans. Antennas Propag.* 69(12), 9021–9025 (2021). <https://doi.org/10.1109/tap.2021.3083820>
32. Lin, B., et al.: Design of a wideband transmissive linear-to-circular polarisation converter based on a metasurface. *Appl. Phys. A* 124(10), 715 (2018). <https://doi.org/10.1007/s00339-018-2135-y>
33. Clendinning, S., et al.: Bandwidth comparison of rectangular and offset cross-slot frequency-selective surface polarisation transformers. *Electron. Lett.* 27(09), 372–374 (2021). <https://doi.org/10.1049/ell2.12141>
34. Zhang, W., Li, B., Zhu, L.: Orthogonal adjacent-order filtering element-based wideband transmissive linear-to-circular polarisation converter. *IEEE Trans. Antennas Propag.* 71(4), 3324–3334 (2023). <https://doi.org/10.1109/tap.2023.3243841>
35. Pouyanfar, N., Nourinia, J., Ghobadi, C.: Multiband and multifunctional polarisation converter using an asymmetric metasurface. *Sci. Rep.* 11(1), 9306 (2021). <https://doi.org/10.1038/s41598-021-88771-x>
36. Ahmed, F., Khan, M.I., Tahir, F.A.: A multifunctional polarisation transforming metasurface for C-X-and K-band applications. *IEEE Antennas Wirel. Propag. Lett.* 20(11), 2186–2190 (2021). <https://doi.org/10.1109/lawp.2021.3065717>
37. Khan, M.I., Khalid, Z., Tahir, F.A.: Linear and circular-polarisation conversion in X-band using anisotropic metasurface. *Sci. Rep.* 9(1), 4552 (2019). <https://doi.org/10.1038/s41598-019-40793-2>
38. Nguyen, T.K.T., et al.: Simple design of efficient broadband multifunctional polarisation converter for X-band applications. *Sci. Rep.* 11(1), 2032 (2021). <https://doi.org/10.1038/s41598-021-81586-w>
39. Tutar, F., Ozturk, G.: An effective metasurface-based linear and circular polarisation converter for C- and X-band applications. *Opt. Mater.* 128, 112355 (2022). <https://doi.org/10.1016/j.optmat.2022.112355>
40. Padmaja Bikkuri, S.D., Sudhakar, A.: Design of low profile multiband reflective polarisation converter for both linear and circular polarised waves. *Prog. Electromagn. Res. Lett.* 97, 61–68 (2021). <https://doi.org/10.2528/piel21022601>
41. Zheng, Q., Guo, C., Ding, J.: Wideband metasurface-based reflective polarisation converter for linear-to-linear and linear-to-circular polarisation conversion. *IEEE Antennas Wirel. Propag. Lett.* 17(8), 1459–1463 (2018). <https://doi.org/10.1109/lawp.2018.2849352>
42. Kaya, Y.: Cheaper, wide-band, ultra-thin, and multi-purpose single-layer metasurface polarisation converter design for C-X-and Ku-band applications. *Symmetry* 15(2), 442 (2023). <https://doi.org/10.3390/sym15020442>
43. Zheng, Q., et al.: Dual-broadband highly efficient reflective multi-polarisation converter based on multi-order plasmon resonant metasurface. *IET Microw. Antennas Propag.* 14(9), 967–972 (2020). <https://doi.org/10.1049/iet-map.2019.0984>
44. Ozturk, U.G.: Ultra-thin, wide-angle and bandwidth-enhanced linear and circular metasurface-based reflection-type polarisation converter at X-band microwave frequency. *J. Electromagn. Waves App.* 36(10), 1423–1435 (2022). <https://doi.org/10.1080/09205071.2022.2029722>
45. Lin, B.-Q., et al.: Multiple-band linear-polarisation conversion and circular polarisation in reflection mode using a symmetric anisotropic metasurface. *Phys. Rev. Appl.* 9(2), 024038 (2018). <https://doi.org/10.1103/physrevapplied.9.024038>
46. Balanis, C.A.: *Antenna Theory: Analysis and Design*. Wiley, New York (2005)
47. Iqbal, A., et al.: Electromagnetic bandgap backed millimeter-wave MIMO antenna for wearable applications. *IEEE Access* 7, 111135–111144 (2019). <https://doi.org/10.1109/access.2019.2933913>
48. Bhattacharyya, S., Ghosh, S., Srivastava, K.V.: A wideband cross polarisation conversion using metasurface. *Radio Sci.* 52(11), 1395–1404 (2017). <https://doi.org/10.1002/2017rs006396>
49. Jia, Y., et al.: Ultra-wideband metasurface with linear-to-circular polarisation conversion of an electromagnetic wave. *Opt. Mater. Express* 8(3), 597–604 (2018)
50. Jiang, Y., et al.: Ultra-wideband high-efficiency reflective linear-to-circular polarisation converter based on metasurface at terahertz frequencies. *Opt. Exp.* 25, 27616–27623 (2017)
51. Jiang, Y., et al.: Broadband linear-to-circular polarisation converter based on phosphorene metamaterial. *Opt. Mater. Exp.* 9(5), 2088–2097 (2019)
52. Xu, J., et al.: Ultra-broadband linear polarisation converter based on anisotropic metasurface. *Opt Express* 26(20), 26235–26241 (2018)
53. Mustafa, M.-E., Tahir, F.A., Amin, M.: Broadband waveplate operation by orthotropic metasurface reflector. *J. Appl. Phys.* 126(18) (2019). <https://doi.org/10.1063/1.5122768>

**How to cite this article:** Islam, K. M. R., et al.: A compact single-layer reflective metasurface for high-efficiency polarisation conversion applications in C and X bands. *IET Microw. Antennas Propag.* 1–13 (2024). <https://doi.org/10.1049/mia2.12465>